

## MIT Open Access Articles

*Molecular simulation of flow-enhanced nucleation of polyethylene crystallites in biaxial flows*

The MIT Faculty has made this article openly available. **Please share** how this access benefits you. Your story matters.

**Citation:** Chinmay S Gangal, Gregory C. Rutledge; Molecular simulation of flow-enhanced nucleation of polyethylene crystallites in biaxial flows. J. Chem. Phys. 21 April 2024; 160 (15): 154904.

**Published Version:** 10.1063/5.0203993

**Publisher:** AIP Publishing

**Permanent Link:** <https://hdl.handle.net/1721.1/164214>

**Version:** Final published version: final published article, as it appeared in a journal, conference proceedings, or other formally published context

**Terms of use:** <https://creativecommons.org/licenses/by/4.0/>



# Molecular simulation of flow-enhanced nucleation of polyethylene crystallites in biaxial flows

Cite as: *J. Chem. Phys.* **160**, 154904 (2024); doi: [10.1063/5.0203993](https://doi.org/10.1063/5.0203993)

Submitted: 18 February 2024 • Accepted: 1 April 2024 •

Published Online: 17 April 2024



View Online



Export Citation



CrossMark

Chinmay S Gangal  and Gregory C. Rutledge<sup>a)</sup> 

## AFFILIATIONS

Department of Chemical Engineering, Massachusetts Institute of Technology, Cambridge, Massachusetts 02139, USA

<sup>a)</sup> Author to whom correspondence should be addressed: [rutledge@mit.edu](mailto:rutledge@mit.edu)

## ABSTRACT

Flow-enhanced nucleation (FEN) of n-pentacontane (C<sub>150</sub>) under biaxial extensional flows of varying strain rate ratios is studied using nonequilibrium molecular dynamics simulation. The nucleation rates thus calculated are used to test previously published FEN models based on invariants of the conformation tensor of Kuhn segments and the extra stress tensor. Models based on the conformation tensor provide a more accurate description of FEN observed in biaxial flow simulations than those based on the extra stress tensor. In addition, the formation of nematic domains previously reported to be stabilized by shear or extensional flow is absent in equibiaxial flows. However, such domains do form in non-equibiaxial flows, and nucleation occurs in these domains preferentially. The shape and orientation of nuclei formed under biaxial flows of various strengths and strain rate ratios are also reported.

© 2024 Author(s). All article content, except where otherwise noted, is licensed under a Creative Commons Attribution (CC BY) license (<https://creativecommons.org/licenses/by/4.0/>). <https://doi.org/10.1063/5.0203993>

## I. INTRODUCTION

Semicrystalline polymers constitute the largest fraction of industrial plastics. They are used for fabrication of fibers, films, packaging, and composites.<sup>1</sup> Production processes for many of these products, such as injection molding, blown-film extrusion, and heat-sealing, involve complex flows coupled with solidification from the melt. The effect of flow on the final structure and properties, especially crystallinity, is complicated. Crystallization involves rearrangement of molecules into ordered regions; flow aids in this ordering through reorientation of polymer chain segments. The amount of stretching and orientation that the flow introduces dramatically affects the crystallization rate and consequent morphology.<sup>2</sup> The evidence for rate enhancement in blown-film processes<sup>3</sup> and changes in morphology in injection molding<sup>4</sup> exemplify this effect of flow, commonly referred to as Flow-Induced Crystallization (FIC). The earliest stage of FIC is Flow-Enhanced Nucleation (FEN), which involves small molecular clusters that arise suddenly in the solution or melt<sup>5</sup> but plays an important role in determining the final morphology of a material.

Many experimental studies have probed the phenomena of FIC and FEN.<sup>6–13</sup> While experiments have provided valuable insights

into these phenomena, their observations are typically indirect. By contrast, computational techniques, such as molecular dynamics simulations, are well suited to resolve the fine spatiotemporal scale of a nucleation event.<sup>14–22</sup> However, to date, only the effects on nucleation due to shear or uniaxial extensional flow fields have been studied. Biaxial extensional flow (BEF) fields are industrially relevant for processes such as blown-film extrusion (BFE), but their effects on polymer crystallization have received only sparse attention.<sup>23–30</sup> Bullwinkle *et al.*<sup>29</sup> studied BFE using small angle light scattering. They modeled FIC but did not specifically study the effects of biaxial flow. Van Drongelen *et al.*<sup>30</sup> measured crystallinity and molecular orientation in BFE using wide-angle x-ray diffraction. They found that the process conditions that lead to high molecular orientation also lead to higher crystallinity. Zhang *et al.*<sup>26</sup> and Chen *et al.*<sup>25</sup> studied experimentally the effect of transient biaxial stretching on the crystallization of polyethylene terephthalate (PET) and natural rubber, respectively. Both reports highlighted the importance of stretch ratio and orientation of amorphous chains. Nie *et al.*<sup>27</sup> modeled nucleation kinetics under biaxial stretching using nonequilibrium molecular dynamics (NEMD) simulations and a coarse-grained model of polyvinyl alcohol; they applied a start-up flow followed by quenching below the melting point with

cessation of flow and showed that the induction time for nucleation correlates with the average local orientation parameter at the final state of strain. However, the simulation protocol employed there convolves the effects of nucleation with relaxation after cessation of flow.

Nicholson and Rutledge<sup>21</sup> examined nucleation rates for a united atom model of n-pentacontane (C150) in steady state shear or uniaxial extensional flow using NEMD simulations with lattice reduction techniques for generalized homogeneous flows. They simulated a range of strain rates and employed an iso-Weissenberg number quench to reduce the effect of the quench on chain conformation. They used these results to test several nucleation rate models proposed in the literature. Each model was classified according to the nature of the independent variable in the model: (a) strain rate, (b) stress, (c) conformation, or (d) free energy. Models based on measures of stress or conformation were found to perform significantly better than the others; in some cases, the two were indistinguishable. They argued that the similarity in performance is a consequence of the stress-optical rule and arises from coaxiality of stress and conformation tensors in shear and uniaxial extensional flow.

In this work, we report the effect of steady state biaxial flow on the orientation of C150 chain segments in the melt state, and in turn on nucleation kinetics, using the methods of Nicholson and Rutledge.<sup>21</sup> Equibiaxial and non-equibiaxial flows are characterized by different ratios of the strain rate in orthogonal directions within the plane of biaxial extension. The orientation of chain segments under these flows is quantified using the conformation tensor and nematic order parameters. Nucleation kinetics under BEF are compared and contrasted with those published previously for uniaxial and shear flows. A model in which FEN is correlated with the  $P_2$  order parameter tensor for Kuhn segments is found to work well under all of the flow conditions studied.

## II. METHODS

### A. Flow simulation

The simulated system consisted of a melt of 100 C150 chains in which each  $\text{CH}_2$  or  $\text{CH}_3$  unit was modeled as a united atom (UA). The force field of Paul, Yoon, and Smith (PYS)<sup>31</sup> with modifications by Waheed *et al.*<sup>32,33</sup> was used for the simulations; it has been shown previously to provide a realistic description of polyethylene melts and crystal nucleation.<sup>34–37</sup>

The LAMMPS software<sup>38</sup> was used to perform all the simulations. The USER-UEF<sup>39</sup> package allows for simulation of steady-state biaxial extensional flows with lattice reduction and remapping of compatible boundary conditions. The package employs the SLLOD equations of motion with boundary conditions as proposed by Dobson<sup>40</sup> and modified by Hunt.<sup>41</sup> A rate-of-deformation tensor as shown in the following equation was imposed in the simulation for biaxial flow:

$$\nabla \mathbf{u} = \begin{bmatrix} \dot{\epsilon}\xi & 0 & 0 \\ 0 & \dot{\epsilon}(1-\xi) & 0 \\ 0 & 0 & -\dot{\epsilon} \end{bmatrix}, \quad (1)$$

where  $0 \leq \xi \leq 1$ . Evidently,  $x$  and  $y$  form the directions of extension and  $z$  is the direction of compression.  $\xi$  equal to 1 or 0 corresponds

to planar extensional flow in the  $x$  or  $y$  direction, respectively;  $\xi = 0.5$  corresponds to equibiaxial flow in the  $xy$  plane. For convenience, we define a strain rate ratio  $\Lambda$  in the plane of extension as

$$\Lambda = \frac{\xi}{1-\xi} \quad (2)$$

and restrict  $\xi$  to the range  $0.5 \leq \xi < 1$ . Under these conditions,  $\Lambda = 1$  corresponds to equibiaxial flow,  $\Lambda > 1$  corresponds to biaxial flow with the major axis of extension in the  $x$  direction, and planar extensional flow in the  $x$  direction is obtained in the limit that  $\Lambda$  becomes very large. An effective strain rate ( $\dot{\gamma}$ ) was computed from the deformation rate tensor according to the following equation:

$$\dot{\gamma} = \sqrt{J_2(\mathbf{D})/2}, \quad (3)$$

where  $\mathbf{D} = \nabla \mathbf{u} + \nabla \mathbf{u}^T$  is the strain rate tensor and  $J_2(\mathbf{D}) = \text{tr}(\mathbf{D}^2)$  is its second invariant. This deformation rate tensor is volume-conserving. However, to accommodate density changes associated with crystallization, the simulations were implemented with a constant stress boundary condition in the compression direction; the average stress in that direction was controlled to be 1 atm. In the absence of crystallization, the change in volume at a constant  $z$ -component of stress averages to zero. For all simulations, the LAMMPS implementation of the Nosé–Hoover thermostat and barostat was used, with time constants of 0.4 and 4 ps, respectively. The equations of motion were integrated using the reversible reference system propagator algorithm (rRESPA)<sup>42</sup> with a 2 fs time step for bonded interactions and a 4 fs time step for nonbonded interactions. More details on the simulation procedure can be found in the work of Nicholson and Rutledge.<sup>21</sup>

For the simulation procedure, a steady state biaxial flow was imposed in the melt state at 440 K. This temperature is above the experimental melting point of 396.4 K for C150.<sup>43</sup> The PYS force field has been shown elsewhere to reproduce experimental melting points for n-alkanes within about  $\pm 2\%$ .<sup>35,44,45</sup> The melt state flow simulation was run for 90 ns to reach the steady state, as confirmed by fluctuation of the Kuhn segment order parameter (defined below) about a steady average. The simulation was run for an additional 750 ns to analyze the melt flow state. 25 snapshots were sampled at intervals of 30 ns for subsequent nucleation studies. This time interval is slightly greater than the Rouse time ( $\tau_R$ ) of 26 ns<sup>36</sup> for C150 at 440 K, ensuring independent, uncorrelated starting configurations. These configurations were then quenched to a crystallization temperature of 280 K, corresponding to a 29% supercooling ( $(T_m - T)/T_m$ ), to initiate crystal nucleation trajectories.  $\tau_R$  for C150 at 280 K is estimated to be 340 ns.<sup>36</sup> The strain rate of the simulation after quenching was chosen such that the Rouse Weissenberg number, defined as  $Wi = \dot{\gamma}\tau_R$ , was the same before and after the quench (an “iso-Weissenberg number quench”). Example strain rates before and after quench are presented in the supplementary material, Table S1. The steady-state NEMD simulations were conducted for strain rate ratios corresponding to  $\Lambda = 1, 1.2, 1.5, 3, \text{ and } 10$ . Out of these simulations, configurations from simulations having  $\Lambda = 1, 1.5, \text{ and } 3$  were used for nucleation simulations, as these were sufficient to draw the conclusions of this work; with further increases in  $\Lambda$ , the deformation approaches planar extensional flow, which is similar to uniaxial extensional flow, for which data already exist.<sup>21</sup>

## B. Analysis methods

First, we define a chord vector  $\mathbf{R}_i$  and a Kuhn segment vector  $\mathbf{R}_{K,i}$  for each united atom  $i$  in the system and their unit vectors  $\mathbf{d}_i$  and  $\mathbf{d}_{K,i}$ , respectively. A Kuhn segment is taken to have  $n_K = 12$  carbon atoms,<sup>46–48</sup> with the vector  $\mathbf{R}_K$  going from the first to the last carbon of the Kuhn segment. The chain ends are treated differently, as shown in the definition in Eq. (5),

$$\mathbf{R}_i = \mathbf{r}_{i+1} - \mathbf{r}_{i-1}, \quad (4)$$

$$\mathbf{R}_{K,i} = \begin{cases} \mathbf{r}_{i+n_K/2} - \mathbf{r}_{i-n_K/2}, & n_K/2 < i \leq n_{mol} - n_K/2 \\ \mathbf{R}_{K,1+n_K/2}, & 1 \leq i \leq n_K/2 \\ \mathbf{R}_{K,n_{mol}-n_K/2}, & n_{mol} - n_K/2 < i \leq n_{mol} \end{cases}, \quad (5)$$

$$\mathbf{d}_i = \mathbf{R}_i / \sqrt{\mathbf{R}_i \cdot \mathbf{R}_i}, \quad (6)$$

and

$$\mathbf{d}_{K,i} = \mathbf{R}_{K,i} / \sqrt{\mathbf{R}_{K,i} \cdot \mathbf{R}_{K,i}}, \quad (7)$$

where  $\mathbf{r}_i$  is the Cartesian coordinate of site  $i$  and  $n_{mol}$  is the total number of UAs in the chain, i.e.,  $n_{mol} = 150$ .

### 1. Crystalline order parameter, clustering, and nucleation rate

The unit chord vector is used to calculate a scalar order parameter  $P_{2,i}$ , by which crystalline UAs are distinguished from noncrystalline UAs,

$$P_{2,i} = \frac{3}{2} \left( (\mathbf{d}_i \cdot \mathbf{d}_j)^2 \right)_{j \in \Gamma_i} - \frac{1}{2}, \quad (8)$$

$$\Gamma_i = \{j : |\mathbf{r}_j - \mathbf{r}_i| < r_{local}\},$$

where  $\Gamma_i$  is the local neighborhood of the  $i$ th UA, comprising all UAs  $j$  within a cutoff distance of  $r_{local} = 1.5\sigma_{LJ} \approx 0.6$  nm from the  $i$ th UA. Any UA that had  $P_{2,i}$  greater than a threshold value  $P_{2,th} = 0.7$  was considered crystalline. These parameter values are consistent with those used by Nicholson and Rutledge for crystallization in flowing systems.<sup>21</sup> Two crystalline UAs within a threshold distance  $r_{th} = 1.3\sigma_{LJ} \approx 0.52$  nm of each other were considered to be a part of the same crystalline cluster. To calculate a nucleation rate, the size of the largest cluster was tracked throughout the simulation. The first-passage time of the largest cluster  $FPT(n)$  (that is, the time after quench at which the largest cluster first reaches a cluster of size  $n$  UAs) was calculated for each of the 25 nucleation runs. Both the mean,  $\tau_{FPT}(n)$ , and standard deviation,  $\sigma_{FPT}(n)$ , of the first passage time (FPT) distribution for the 25 trajectories were calculated. For a Poisson process, the two functions should be equal; however, in simulations where the growth rate of the clusters after nucleation is non-stochastic and measurable on the nucleation time scale,  $\tau_{FPT}(n)$  continues to increase with increasing  $n$ , whereas  $\sigma_{FPT}(n)$  levels off for values of  $n$  several times greater than the critical nucleus size. For this reason, induction time was estimated in this work from the plateau value  $\sigma_{plateau}$  of the standard deviation of the FPT distribution at large  $n$ , as proposed by Shneidman.<sup>49</sup> The nucleation rate was then simply calculated as  $I_s = (\sigma_{plateau} V)^{-1}$ , where  $V = 420.54 \text{ nm}^3$  is

the volume of the system (corresponding to a density of  $0.83 \text{ g/cm}^3$ ). As discussed later, at sufficiently large  $Wi$ ,  $\sigma_{FPT}(n_{max})$  was found not to level off in accordance with classical nucleation. In such cases, the plateau value was estimated as  $\sigma_{plateau} = \langle \sigma_{FPT}(n) \rangle_{150 < n < 300}$ . To estimate the error in nucleation rate, a jackknife or “leave-one-out” approach was used. In this method, nucleation rates were calculated based on all possible combinations of 24 simulations out of the 25. The standard deviation of these nucleation rates was used as the measure of uncertainty for the mean nucleation rate.

### 2. Cluster fractal dimension, shape anisotropy, and orientation

For supercritical crystalline clusters, we characterized the compactness of the cluster using its fractal dimension,  $D_f$ . For this purpose, we followed the box counting algorithm described by Gagnepain and Roques-Carmes<sup>50</sup> and also employed by Nicholson and Rutledge.<sup>39</sup> Briefly, starting with a cubic box of side length  $L$  that just encloses the cluster, the box was further divided into voxels of side length  $\delta = L/2, L/3$ , etc. For a given  $\delta$ , the number of voxels  $Q(\delta)$  that intersect with any part of a UA in the cluster was counted.  $D_f$  was then determined from the slope of  $-\log(Q(\delta))$  vs  $\log(\delta)$  in the range  $1 \text{ nm} < \delta < \sigma_{LJ}$ , where  $\sigma_{LJ}$  is the Lennard-Jones radius of a UA.  $D_f$  was found to be not very sensitive to the range over which  $\delta$  was averaged (the 1 nm cutoff is chosen for consistency). For a three-dimensional object (such as our nuclei),  $D_f = 3$  for an object that is compact and completely fills space.  $D_f < 3$  for clusters that are not compact and space-filling.

The relative shape anisotropy ( $\kappa^2$ ) of a supercritical crystalline cluster was computed from the eigenvalues ( $\lambda_1 > \lambda_2 > \lambda_3$ ) of its gyration tensor as follows:

$$\kappa^2 = 1 - 3 \frac{\lambda_1 \lambda_2 + \lambda_2 \lambda_3 + \lambda_3 \lambda_1}{(\lambda_1 + \lambda_2 + \lambda_3)^2}. \quad (9)$$

$\kappa^2 = 1$  for a very thin cylinder, and  $\kappa^2 = 0$  for a perfect sphere.

For each simulation,  $D_f$ ,  $\kappa^2$ , and  $n_{max}$ , the size of the largest cluster, were each averaged over five consecutive 3 ns windows, and then,  $\langle D_f \rangle$  and  $\langle \kappa^2 \rangle$  were plotted against  $n_{max}$ . For each biaxial flow mode ( $Wi$ ,  $\Lambda$ ), the results for 25 simulations were binned, and the mean and standard deviation of each bin were plotted vs  $\langle n_{max} \rangle$  for that bin.

The orientation of the cluster was characterized by the orientation of the chain stems within the cluster. Chain molecules, such as C150 and polyethylene, crystallize predominantly in a planar zig-zag conformation so that the stem direction is well approximated by the average direction of the chord vectors within the crystalline cluster. This direction is the director of the orientation tensor,

$$\mathbf{S}_{cluster} = \langle \mathbf{d}_i \mathbf{d}_i \rangle_{i \in cluster}, \quad (10)$$

which is computed by diagonalizing  $\mathbf{S}_{cluster}$ ; the director is then the eigenvector  $\mathbf{e}_1$  associated with the largest eigenvalue of  $\mathbf{S}_{cluster}$ . The vector  $\mathbf{e}_1$  was calculated for the largest cluster the first time it crossed  $n = 200$ . The choice of  $n = 200$  is somewhat arbitrary so long as it is large enough to ensure the clusters are supercritical; in any case, the results were not sensitive to  $n$  for any reasonable choice.

### 3. Melt state structure

Kuhn segment vectors are used to characterize the structure of the melt under biaxial flow conditions prior to quenching. A useful starting point is the Kuhn segment conformation tensor ( $\mathbf{C}_K$ ), defined as

$$\mathbf{C}_K = \frac{\langle \mathbf{R}_K \mathbf{R}_K \rangle}{R_{K,0}^2}, \quad (11)$$

where the brackets indicate averaging over  $\mathbf{R}_{K,i}$  for all UA sites in the system.  $R_{K,0}^2 = \text{tr}(\langle \mathbf{R}_K \mathbf{R}_K \rangle_0)$  is the mean squared Kuhn segment length at equilibrium in the absence of flow. The conformation tensor can be decomposed as  $\mathbf{C}_K = \lambda_K^2 \mathbf{S}_K$ , where  $\lambda_K$  is a scalar stretch factor,  $\lambda_K^2 = \text{tr}(\mathbf{C}_K)$ , and  $\mathbf{S}_K$  is a tensorial orientation factor. The global nematic Kuhn segment order tensor,  $\mathbf{P}_{2,K}$ , is then given by

$$\mathbf{P}_{2,K} = \frac{1}{2}(3\mathbf{S}_K - \mathbf{I}), \quad (12)$$

where  $\mathbf{I}$  is the identity matrix. The second invariant of this nematic order tensor  $J_2(\mathbf{P}_{2,K})$  has been shown previously to provide a good measure for the effect of flow-enhanced nucleation in shear and uniaxial extension.<sup>21</sup>

To distinguish UAs within the melt state that belong to a flow-stabilized nematic phase that is distinct from a melt phase that is merely anisotropic due to the presence of flow, we use a combination of local order parameters based on Kuhn segment vectors. Analogous to the order parameter for crystalline UAs [Eq (8)], we define the first of these local order parameters using a scalar Kuhn segment order parameter  $P_{2,K,i}$  for nematic UAs in the melt,

$$P_{2,K,i} = \frac{3}{2} \langle (\mathbf{d}_{K,i} \cdot \mathbf{d}_{K,j})^2 \rangle_{j \in \Gamma_i} - \frac{1}{2}, \quad (13)$$

where  $\Gamma_i$  is the local neighborhood of the  $i$ th UA as defined in Eq. (8).

For the second of these local order parameters, we follow the approach of Nicholson and Rutledge,<sup>22</sup> who introduced a co-alignment parameter to gauge the degree to which Kuhn segments associated with sites  $j$  in the local neighborhood of site  $i$  are co-aligned with the nematic director of that neighborhood (the directrix). Analogous to the cluster orientation analysis, a local orientation tensor for Kuhn segments is defined as

$$\mathbf{S}_{K,i} = \langle \mathbf{d}_{K,j} \mathbf{d}_{K,j} \rangle_{j \in \Gamma_i}, \quad (14)$$

where, again,  $\Gamma_i$  is the local neighborhood of the  $i$ th UA as defined in Eq. (8) and the same  $r_{\text{local}}$ . The director  $\bar{\mathbf{d}}_{K,i}$  for the neighborhood of the  $i$ th UA is the eigenvector ( $\mathbf{e}_{1,K}$ ) of  $\mathbf{S}_{K,i}$  associated with its largest eigenvalue. The co-alignment parameter is then 1 minus the variance of Kuhn segment vectors with respect to the director for the local neighborhood of the  $i$ th UA, that is,

$$v_{K,i} = 1 - \left[ \langle |\mathbf{d}_{K,j} \cdot \bar{\mathbf{d}}_{K,i}|^2 \rangle_{j \in \Gamma_i} - \langle |\mathbf{d}_{K,j} \cdot \bar{\mathbf{d}}_{K,i}| \rangle_{j \in \Gamma_i}^2 \right]. \quad (15)$$

Nicholson and Rutledge<sup>22</sup> showed that two-dimensional distributions of  $P_{2,K,i}$  and  $v_{K,i}$  split into two distinct peaks above a certain  $Wi$  for both uniaxial and shear flows. The peak associated

with the lower values of  $P_{2,K,i}$  and  $v_{K,i}$  was dubbed “flow-oriented,” whereas the peak associated with higher values of  $P_{2,K,i}$  and  $v_{K,i}$  was dubbed “nematic.” Nematic UAs in the melt are those belonging to the nematic peak in this two-dimensional distribution.

Finally, we employ a memory function that remembers from which domains (nematic or flow-oriented) the sites that are crystalline at a later time  $t$  originated. Following Nicholson and Rutledge,<sup>22</sup> we define a memory function  $Z^L(t)$ ,

$$Z^L(t) = \langle L_{i,0} \rangle_{i: P_{2,K,i}(t) > P_{2,th}}, \quad (16)$$

where  $L_{i,0}$  is a measure of order for the  $i$ th UA in the melt at time zero. For example,  $L_{i,0}$  is some function of  $P_{2,K,i,0}$  and  $v_{K,i,0}$  used to identify UAs within nematic domains in the melt at the time of quench ( $t = 0$ ); in this work, we use  $L_{i,0} = v_{K,i,0}$ , as explained later.  $Z^{v_K}(t)$  is then the average of  $v_{K,i,0}$  for all UAs that are crystalline at time  $t$ . Again,  $P_{2,th} = 0.7$  is used to distinguish sites that are crystalline. Basically,  $Z^{v_K}(t)$  averages the value of  $v_K$  at time 0 for those sites that are crystalline at time  $t$ . A function  $W^{v_K}(n)$  can then be defined based on  $Z^{v_K}(t)$  as

$$W^{v_K}(n) = \left\langle Z^{v_K}(t) \middle| \sum_i x_i = n \right\rangle_t, \quad (17)$$

where  $x_i$  is 1 if the  $i$ th UA is crystalline and 0 otherwise. Thus,  $W^{v_K}(n)$  is the average value of  $Z^{v_K}(t)$  for all simulation snapshots (i.e., all times) in which the total number of crystalline UAs is  $n$ , or crystallinity  $\chi = n/N$ . In the limit that  $\chi$  goes to 1,  $W^{v_K}(n)$  necessarily converges to  $\langle v_{K,i,0} \rangle$ , the system average at the time of quench,  $t = 0$ . However, if nucleation occurs primarily within nematic domains (i.e., domains with higher value of  $v_K$ ),  $W^{v_K}(n)$  takes values of  $v_K$  higher than the system average for small  $n$ , or vice versa if nucleation occurs primarily in flow-oriented domains. Thus, this definition of  $W^{v_K}(n)$  readily shows whether nucleation occurs preferentially in nematic domains or flow-oriented domains. More details on this function can be found in the work of Nicholson and Rutledge.<sup>22</sup>

## III. RESULTS AND DISCUSSION

### A. Kuhn segment orientation in the melt

The imposition of flow induces orientation of the polymer chain segments to varying degrees in the melt state at 440 K. The degree of orientation was characterized by the second invariant of the global nematic Kuhn segment order tensor,  $J_2(\mathbf{P}_{2,K})$ , which can range between 0 and 1.5. This second invariant is plotted vs  $Wi$  in Fig. 1 for the different flow conditions. The uniaxial extensional flow imposes the highest degree of orientation among all flows studied.  $J_2(\mathbf{P}_{2,K})$  is approximately zero at low  $Wi < 1$ , indicative of isotropic melts at small strain rates.  $J_2(\mathbf{P}_{2,K})$  begins to increase around  $Wi = 1$ , indicative of oriented melts, and then to level off above  $Wi = 10$ , as orientation becomes saturated. The same qualitative behavior is observed for the biaxial flows, but with  $J_2(\mathbf{P}_{2,K})$  being lower for the lower strain rate ratio in the range of  $\Lambda = 10$  to 1, with the last corresponding to equibiaxial flow. The shear flow curve overlaps approximately the curve for biaxial flow at  $\Lambda = 1.2$ . These behaviors show that orientation can vary over a wide range under biaxial flow conditions, from orientations weaker than in shear flow for

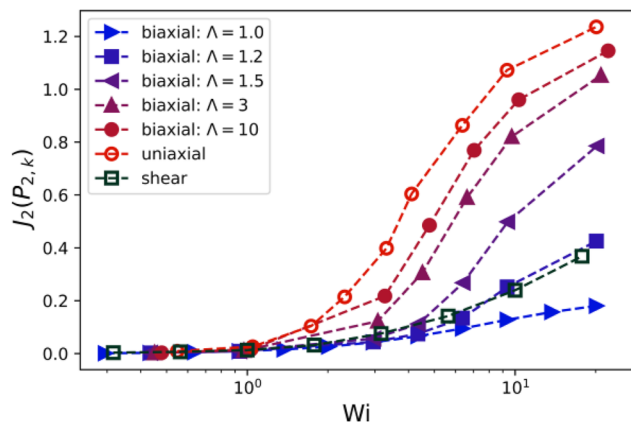


FIG. 1. Average orientation of Kuhn segments in a melt at 440 K as a function of Weissenberg number,  $Wi$ , for different states of flow.

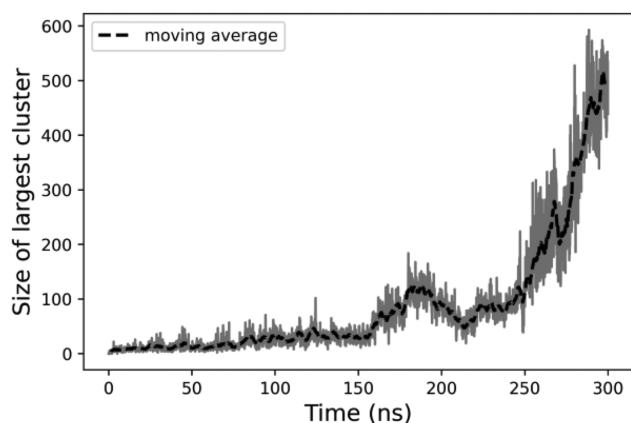


FIG. 2. Size of the largest cluster for equibiaxial flow ( $\Lambda = 1$ ) at  $Wi = 0.30$ . The dashed line indicates the window average over 3 ns intervals.

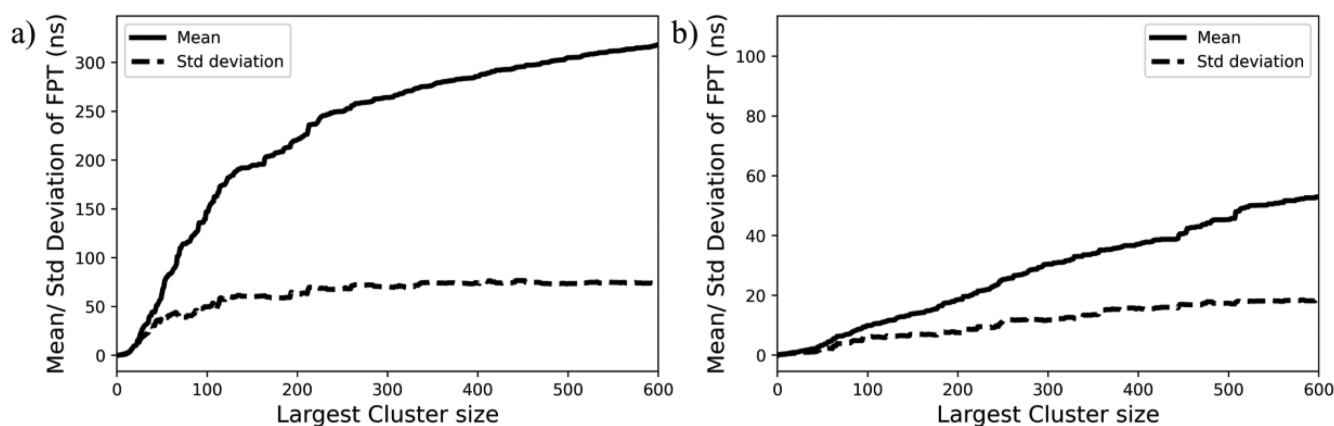


FIG. 3. Mean and standard deviation of first passage time distribution of the largest cluster for equibiaxial flow ( $\Lambda = 1$ ) at (a)  $Wi = 0.30$  and (b)  $Wi = 9.33$ .

equibiaxial flow to orientations approaching that in uniaxial extension for strongly non-equibiaxial flows.

## B. Nucleation rate

To study nucleation kinetics, 25 independent configurations from the melt flow state were quenched to a crystallization temperature  $T_c = 280$  K at constant  $Wi$  (Table S1 in the supplementary material shows typical strain rates before and after the quench). Figure 2 shows the size of the largest crystalline cluster as a function of time after quench for a typical trajectory. The first passage time (FPT) of the largest cluster in the system was tracked for each of the 25 nucleation simulations to create a first-passage time distribution, FPTD. Figure 3 shows the mean and standard deviation,  $\tau_{\text{FPT}}$  and  $\sigma_{\text{FPT}}$ , of the FPT distribution as a function of the size,  $n$ , of the largest cluster for both small and large  $Wi$ . At small  $Wi$  [Fig. 3(a)],  $\sigma_{\text{FPT}}$  levels off at the end of the stochastic nucleation process, whereas  $\tau_{\text{FPT}}$  continues to increase as growth processes become important for supercritical clusters. For sufficiently large  $Wi$  [Fig. 3(b)], neither  $\tau_{\text{FPT}}$  nor  $\sigma_{\text{FPT}}$  levels off, indicative of a breakdown of classical nucleation theory, which is consistent with previously reported observations.<sup>22</sup> For this reason,  $\sigma_{\text{FPT}}$  was evaluated for a fixed range of cluster sizes that was deemed to be only slightly supercritical ( $150 < n < 300$ ), as described in Sec. II. This range was also chosen for consistency with prior work.<sup>21</sup>

Figure 4 shows the nucleation rate as a function of  $Wi$  for different flow conditions. The nucleation rate,  $I_S$ , increases with increasing  $Wi$  for all flows, indicative of FEN. At low  $Wi < 1$ , the increase in the nucleation rate is approximately independent of the flow conditions, whereas for  $Wi > 1$ , the nucleation rate is strongly dependent on the flow conditions. As was the case for  $J_2(P_{2,K})$  in Fig. 1,  $I_S$  decreases with the decreasing strain rate ratio between 3 and 1 in BEF at any given  $Wi$ , from the highest values for strongly non-equibiaxial flow to the lowest values for equibiaxial flow. For the case of equibiaxial flow,  $\Lambda = 1$ , the nucleation rate appears to level off around  $Wi = 10$ . This behavior is a preliminary indication that nucleation rate correlates with chain segment orientation. This correlation is explored quantitatively in the discussion of FEN models that follows.

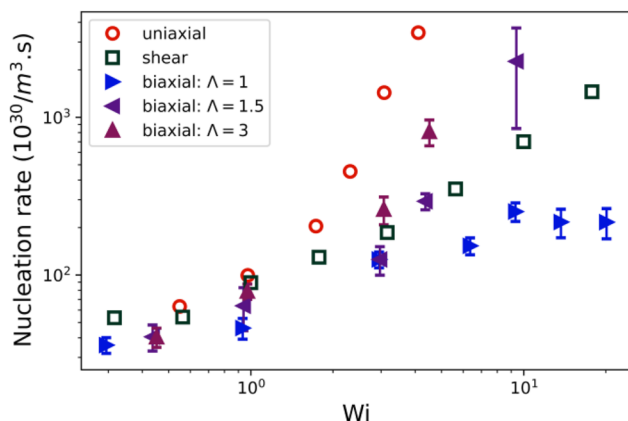


**FIG. 4.** Nucleation rates of the C150 system at 280 K as a function of Weissenberg number,  $Wi$ , for different states of flow. The error bars are jackknife errors from 25 runs. The uniaxial and shear flow nucleation rates are from Ref. 21.

### C. Comparison of FEN models

Figure 5 shows the correlation between the second invariants of the extra stress tensor  $\tau = \sigma - P_{ext}\mathbf{I}$ , where  $\sigma$  is the stress tensor and  $P_{ext}$  is the externally applied pressure (1 atm in our case), for shear, uniaxial, and biaxial flows over a wide range of  $Wi$ . The superposition of data for shear and uniaxial flow is indicative of the stress-optical rule and the coaxiality mentioned in the Introduction. Also shown in Fig. 5 are the dependence of these second invariants for the more general case of biaxial extensional flows for three different strain rate ratios. The biaxial flow data do not superpose. At low  $Wi$  (where the second invariants are small), the biaxial data are shifted upward relative to the shear and uniaxial data, indicative of elevated extra stresses in biaxial flows. At high  $Wi$ , the results for non-equibiaxial flows parallel the uniaxial flow case, whereas the equibiaxial data deviate toward still higher levels of

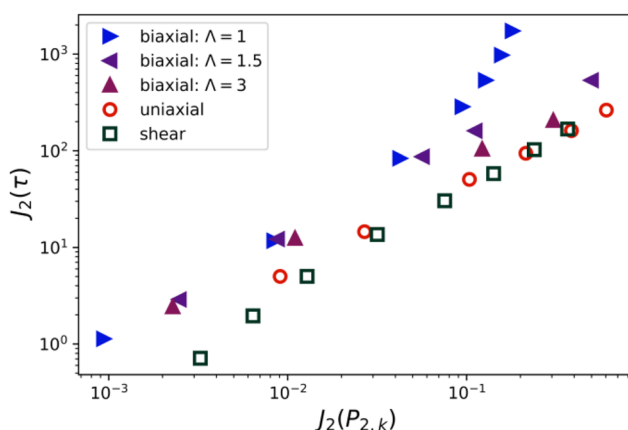


**FIG. 5.** Log–log plot of the second invariant of the extra stress tensor vs that of the Kuhn segment nematic order tensor. The data for shear and uniaxial extensional flow superpose, whereas those for biaxial flows do not.

extra stress. Evidently, significant deviations from the stress-optical rule are manifested in biaxial flows at large  $Wi$ .

Next, we re-examine the stress- and conformation-based models previously studied by Nicholson and Rutledge<sup>21</sup> using nucleation rates obtained by NEMD simulations of C150 in the more general case of biaxial flows. For conformation, we choose a model based on the second invariant of the  $\mathbf{P}_{2,K}$  tensor,

$$I_s = I_{s,q} \exp \left[ \theta_K \sqrt{J_2(\mathbf{P}_{2,K})} \right]. \quad (18)$$

$\theta_K$  is a model parameter. The quiescent nucleation rate  $I_{s,q}$  can be treated as a second model parameter, or it can be determined independently by simulation of nucleation in quiescent systems, as done by Yi *et al.*<sup>36</sup> Here, we treat  $I_{s,q}$  as a model parameter, but the value obtained is of the same order of magnitude as the independently determined value. For stress, we choose a model based on the extra stress tensor,

$$I_s = I_{s,q} \exp \left[ \theta_S \sqrt{J_2(\tau)} \right]. \quad (19)$$

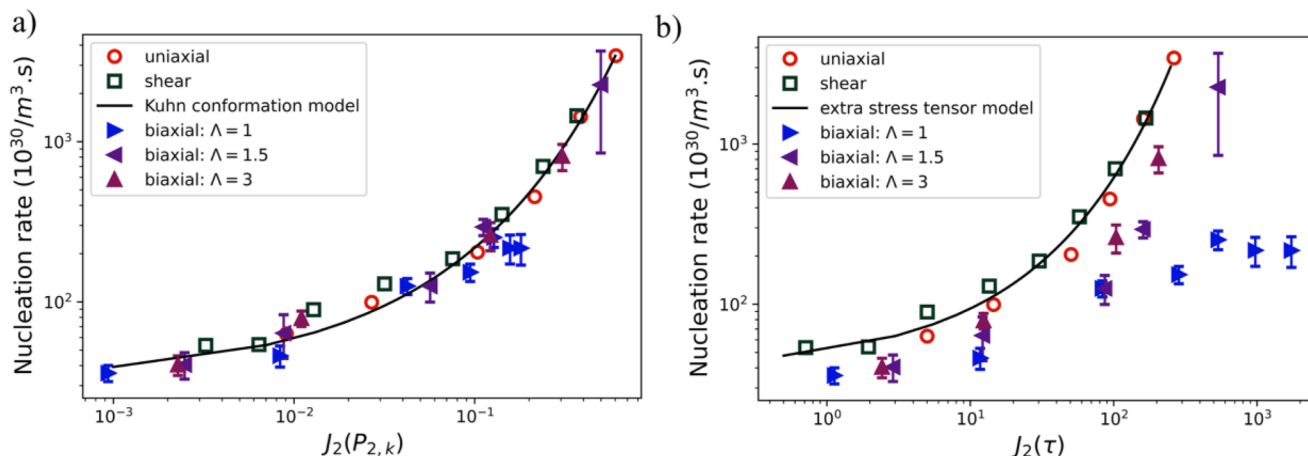
Figure 6(a) shows the nucleation rate for shear, uniaxial, and biaxial flow conditions at three different strain rate ratios, plotted as a function of  $J_2(\mathbf{P}_{2,K})$ . Also shown is the conformation-based model for nucleation rate fitted to all the data points shown in the plot. The model parameters found in this study,  $I_{s,q} = 32.46 \times 10^{30} \text{ m}^{-3} \text{ s}^{-1}$  and  $\theta_K = 6.01$ , are similar to the values reported earlier based on uniaxial and shear data alone ( $I_{s,q} = 38.5 \times 10^{30} \text{ m}^{-3} \text{ s}^{-1}$  and  $\theta_K = 5.79$ ).<sup>21</sup> The model based on the nematic order tensor, Eq. (18), provides a good description of all the data from NEMD simulations for shear, uniaxial, and biaxial flow conditions.

Figure 6(b) shows the same data for the nucleation rate plotted as a function of  $J_2(\tau)$ . Clearly, the data do not collapse onto a single curve, and no single parameterization can describe all the data. The model based on the extra stress tensor, Eq. (19), using parameters reported by Nicholson and Rutledge,<sup>21</sup> is also shown. The nucleation rates for the three biaxial flows follow a similar trend as the model at low  $Wi$  but deviate at high  $Wi$ , indicating a reduced sensitivity of the nucleation rate to extra stress at large applied stresses. This deviation reveals that the extra stress tensor is not as robust as the Kuhn segment order parameter to correlate FEN.

In their experimental study of strain-induced crystallization of natural rubber, Chen *et al.*<sup>25</sup> observed that crystallization did not occur under biaxial stretching conditions for stretch ratios less than 1.6. This suppression of crystallization was attributed to frustration in the alignment of amorphous segments under nearly equibiaxial stretch, which is consistent with the low levels of Kuhn segment orientational order observed under equibiaxial flow conditions for all strain rates ( $Wi$ ) in the current work (Fig. 1). The low levels of orientational order achieved, despite the application of relatively high  $Wi$  (and correspondingly high applied stress, as shown in Fig. S2 of the supplementary material) seems to be indicative of this frustration. As the strain rate ratio increases, a dominant direction of extension emerges and the strain rate required to realize a given amount of orientation decreases.

### D. Cluster shape

The post-critical nuclei can be observed to understand the effect of flow on the shape and morphology of these nuclei. However,



**FIG. 6.** Nucleation rate  $I_s$  for shear, uniaxial, and biaxial flow conditions at three different strain rate ratios. (a)  $I_s$  vs  $J_2(P_{2,K})$ , where the solid curve is the linear least squares best fit to all the data using the nucleation rate model based on the nematic order tensor, Eq. (18). (b)  $I_s$  vs  $J_2(\tau)$ , where the solid curve shows the linear least squares best fit to shear and uniaxial data reported by Ref. 21 using the nucleation rate model based on the extra stress tensor, Eq. (19). The error bars are jackknife errors from 25 runs.

calculating the shape metrics from a single snapshot can be misleading since short-lived appendages appear and disappear with some frequency. Figure 7 shows examples of nuclei showing all UAs appearing as part of the largest cluster in a 3 ns window. The UAs that have low persistence are more transparent and yellow. Within 3 ns, these nuclei can fluctuate about the same shape [Figs. 7(a) and 7(b)], have short-lived appendages [Figs. 7(c) and 7(d)], or consider two nuclei that are close to each other [Figs. 7(e) and 7(f)]. Thus, averaging shape metrics (as detailed in Sec. II) gives us a better estimate of the persistent part of the nuclei. More details on the averaging and rendering of Fig. 7 are given in the supplementary material.

Fractal dimensions and relative shape anisotropy are plotted as functions of cluster size in Figs. 8 and 9, respectively. The fractal dimension values are all above 2.5, which for a three-dimensional object means that they are largely space filling. The shape anisotropy values are also below 0.5, with most of them being in the 0.2–0.3 range. Thus, the nuclei are mostly spherical and not cylindrical or rod-like. For a given  $Wi$ , increasing the size of nucleus decreases the fractal dimension, but the anisotropy is largely unaffected. Thus, the larger nuclei are not as completely filled as the smaller ones and become slightly more spherical as they grow. On the other hand, increasing  $Wi$  decreases the fractal dimension of nuclei and increases their shape anisotropy. Thus, slower flows allow nuclei to be more completely filled and more spherical in shape. Slower flows lead to slower formation of nuclei, which gives polymer chains more time to organize themselves in more filled and spherical nuclei. Comparing between  $\Lambda = 1$  and  $\Lambda = 3$ , there are no significant differences in shape metrics. Thus, we can say that the type of biaxial flow does not affect the shape of nuclei for the flow conditions examined in this work.

### E. Cluster orientation

Flow biases the orientation of Kuhn segments in the melt, so it may be expected that the orientation of crystallites is similarly

biased. The crystallite orientation can be conveniently characterized by the direction cosines of the director of  $\mathbf{S}_{\text{cluster}}$  with respect to the axes of flow. Figure 10(a) shows the relevant section of a triangle plot of the square of the direction cosines of the cluster director, averaged over clusters of size (or  $n$ ) approximately equal to 200 from 25 trajectories. To show the variation in orientations of these 25 nuclei, the director is projected onto the plane of extension ( $xy$  plane). The angle this projection makes with the  $x$  axis is called  $\theta_{\text{proj}}$  and the mean and standard deviation of  $\theta_{\text{proj}}$  is shown in Fig. 10(b). The data point for crystallite orientation in the absence of flow (quiescent crystallization) lies close to the centroid of the triangle in Fig. 10(a), showing that crystal stems have no orientation preference in this case. With increasing  $Wi$ , all data points for biaxial flows are shifted toward the  $xy$  plane. The data points for equibiaxial flow (in blue) are all approximately equidistant from the  $x$  and  $y$  vertices, but with a very broad distribution of values in the angle  $\theta_{\text{proj}}$ . Figure 10(b) confirms that there is a large variation in orientation in the  $xy$  plane for the case of  $\Lambda = 1$ . Taken together, these observations indicate that the clusters are randomly oriented in the  $xy$  plane for all  $Wi$  when  $\Lambda = 1$ . For strain rate ratios  $\Lambda > 1$ , the crystallites orientation shifts toward the  $x$  axis with increasing  $Wi$ , and the distribution of orientation becomes rather narrow. Thus, crystallites in strong biaxial flows with  $\Lambda > 1$  are oriented along the  $x$  axis (i.e., the axis of strongest extension). Some example angle distributions are shown in the supplementary material, Fig. S3.

### F. Nematic ordering in melt phase

Following the method of Nicholson and Rutledge,<sup>22</sup> the formation of nematic domains in the melts under biaxial flow is examined using two-dimensional distributions of the populations of UAs as functions of the Kuhn segment order parameters  $v_K$  and  $P_{2,K}$ . For  $\Lambda > 1$ , these distributions exhibit two peaks above a critical  $Wi$ . This behavior is shown in Fig. 11.

Although the individual order parameters are clearly correlated, projections of the distributions onto the individual order

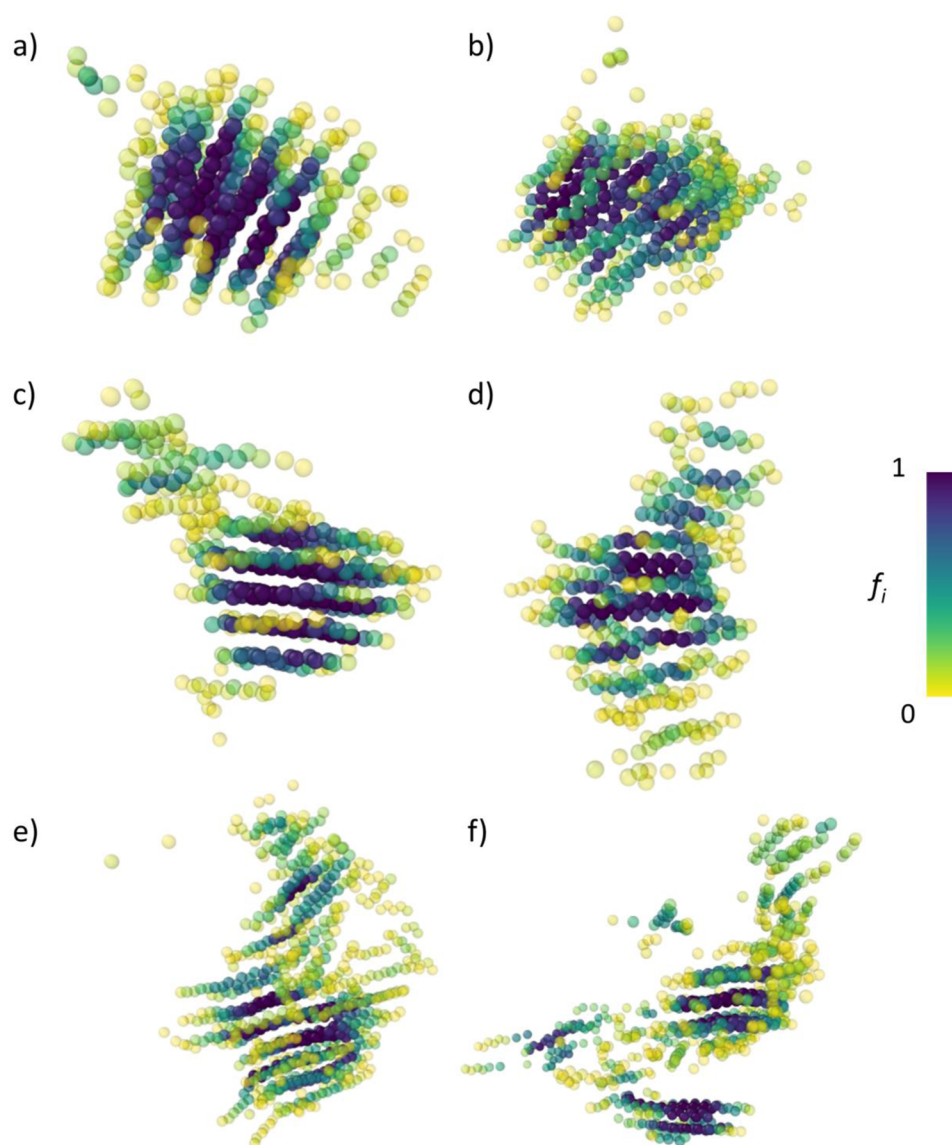


**FIG. 7.** Examples of various nuclei from equibiaxial ( $\Lambda = 1$ ) flow simulations. All UAs appearing in the largest nucleus in a 3 ns window are shown here.  $f_i$  is the fraction of time in this window that a UA  $i$  was part of the largest nucleus. More details on calculation of  $f_i$  are provided in the supplementary material.

parameter planes reveal that the two distinct peaks are more evident as a function of  $v_K$  than  $P_{2,K}$ . Thus, Fig. 12 shows projections of the UA populations on the  $v_K$  plane for a range of  $Wi$  at three different strain rate ratios,  $\Lambda = 1.0, 1.5,$  and  $3.0$ . Figure 12(a) and the first column of Fig. 11 show that equibiaxial flow does not give rise to the nematic order peak, and only a shoulder can be seen at the highest  $Wi$ . On the other hand, higher strain rate ratios [Figs. 12(b) and 12(c) and the second and third columns of Fig. 11] show bimodal distributions. The lower valued peak is designated the “flow-oriented” population, and the higher valued peak is designated the “nematic” population.

Figure 13 shows the function  $W^{v_K}(n)$  as a function of  $n$  for several combinations of  $Wi$  and  $\Lambda$ . In all cases, one observes  $W^{v_K}(n) > \langle v_{K,i,0} \rangle_i$  for all  $n$ , with  $W^{v_K}(n)$  approaching  $\langle v_{K,i,0} \rangle_i$  in the limit that  $n$  approaches  $N$ , the total number of UAs in the system. This observation confirms that nucleation occurs preferentially in nematic domains as measured by  $v_K$ .

Nie *et al.*<sup>27</sup> performed NEMD simulations of a polyvinyl alcohol (PVA) undergoing biaxial stretch; they also reported a spatial correlation between the more ordered sites in the melt and the sites found in crystal nuclei. Using all-atom MD simulations of polyethylene (C1000) under shear flow, Tang *et al.*<sup>51</sup> concluded that

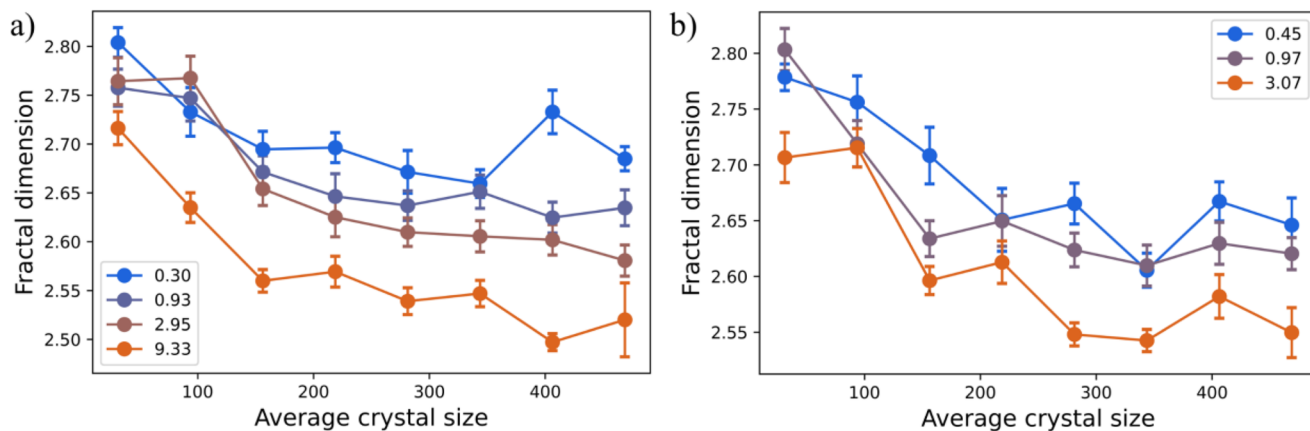


FIG. 8. Fractal dimension of nuclei for (a)  $\Lambda = 1$  and (b)  $\Lambda = 3$ . The colors represent different  $Wi$ . The error bars are standard error.

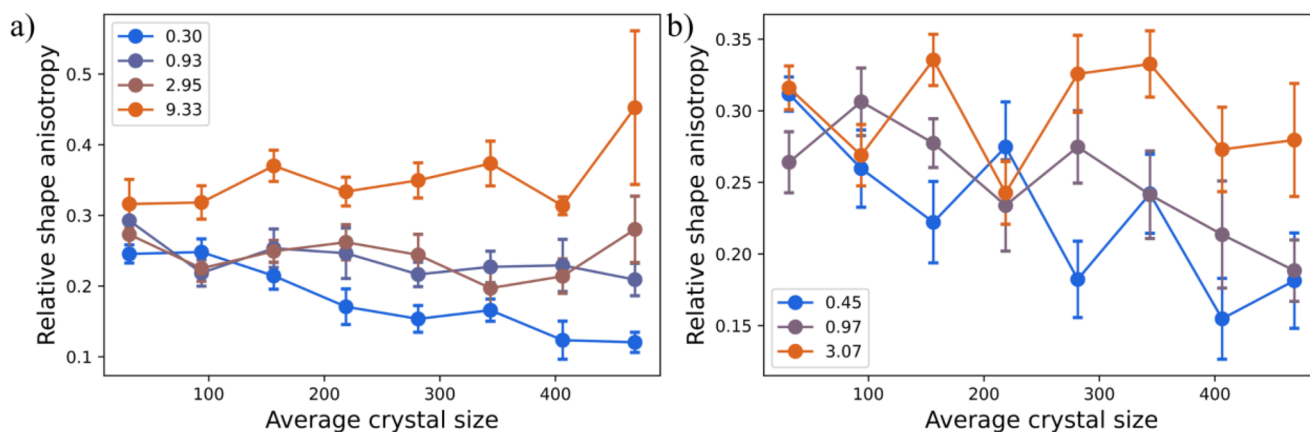


FIG. 9. Relative shape anisotropy of nuclei for (a)  $\Lambda = 1$  and (b)  $\Lambda = 3$ . The colors represent different  $Wi$ . The error bars are standard error.

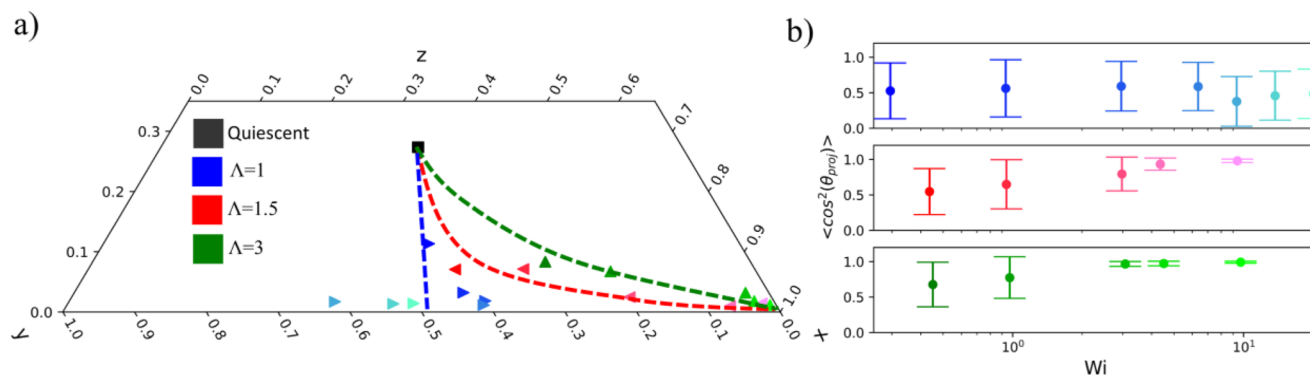
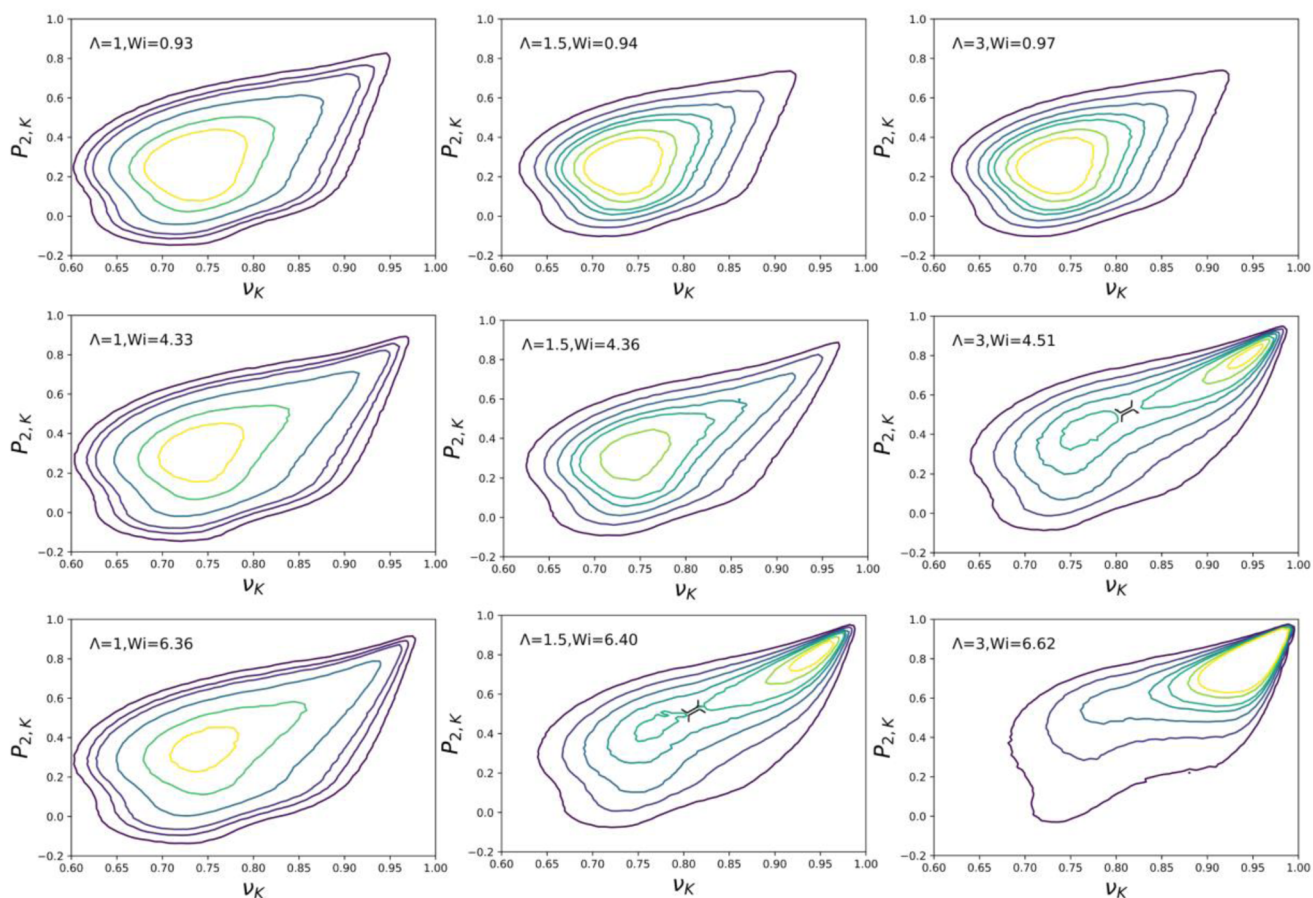
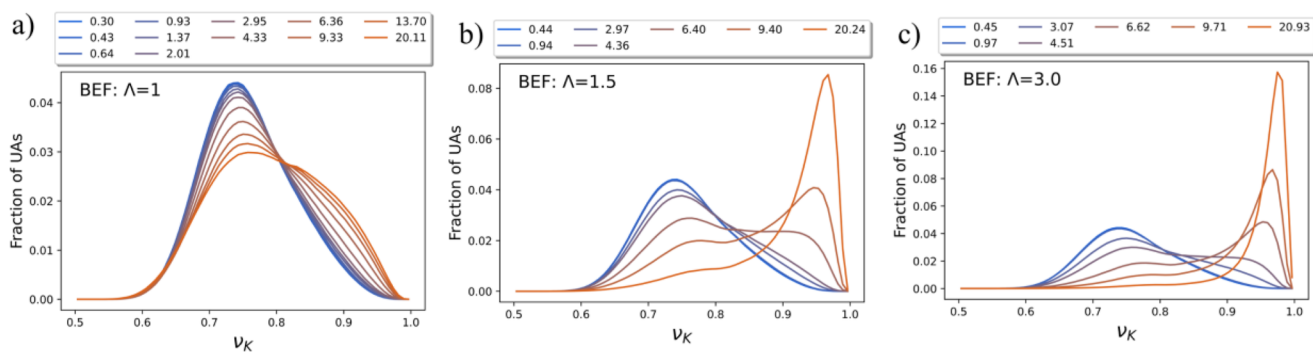


FIG. 10. (a) Section of a triangle plot with each vertex being  $\langle \cos^2 \theta_i \rangle$ , where  $\theta_i$  is the angle made by the director of crystal stems with axis " $i$ " ( $i \in \{x, y, z\}$ ). Different colors show different  $\Lambda$  with  $Wi$  increasing as one goes from the darkest shade of that color to the lightest. The dotted lines are meant as guides to the eye and are not mathematical fits. (b)  $\langle \cos^2 \theta_{proj} \rangle$  as a function of  $Wi$ , where  $\theta_{proj}$  is the angle made by the projection of the director in the  $xy$  plane with the  $x$  axis. The error bars show the standard deviation from 25 nuclei studied. The colors match (a) here.



**FIG. 11.** Two-dimensional distributions of nematic order parameter ( $P_{2,K}$ ) and coalignment parameter ( $\nu_K$ ) for biaxial flow. In the grid of distributions shown,  $Wi$  increases from top to bottom and  $\Lambda$  increases from left to right. A marker is used to indicate the approximate position of the saddle point between the two peaks in the distribution for the two subfigures where the presence of two populations is unambiguous.



**FIG. 12.** Coalignment parameter ( $\nu_K$ ) distribution for biaxial flow with (a)  $\Lambda = 1$  (equibiaxial), (b)  $\Lambda = 1.5$ , and (c)  $\Lambda = 3$  with varying  $Wi$ . The colors represent data for different  $Wi$ , with blue being the weakest flow and orange being the strongest flow.

FEN is a two-step process in which nucleation occurs in regions of higher density. The higher density of these regions was attributed to their being more ordered. Thus, similar to this work, they observe nucleation occurring preferentially from more ordered regions.

Figure 14 shows a phase diagram based on whether a nematic phase was observed in the simulations at 440 K. Each of the biaxial flows (except  $\Lambda = 1$ ) shows a minimum  $Wi$  for the formation of the nematic phase.  $Wi$  at which nematic domains emerge decreases

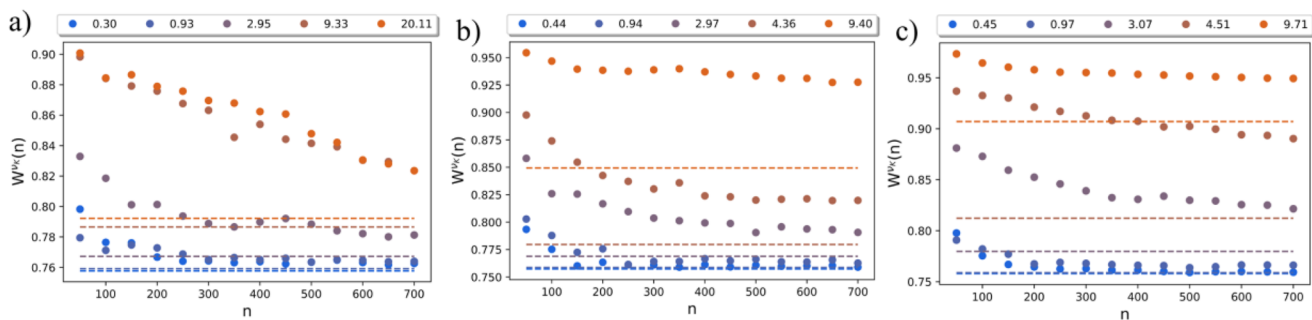


**FIG. 13.** Dependence of  $W^{K}(n)$  on nucleus size ( $n$ ) for biaxial flow at several values of  $Wi$ . (a)  $\Lambda = 1$  (equibiaxial), (b)  $\Lambda = 1.5$ , and (c)  $\Lambda = 3$ . The horizontal dashed lines correspond to  $\langle v_{K,i,0} \rangle$ , the limiting values of  $W^{K}(n)$  as  $n/N$  goes to 1. The color for data and dashed lines correspond to different  $Wi$ , with blue being the smallest  $Wi$  and orange being the largest  $Wi$ .

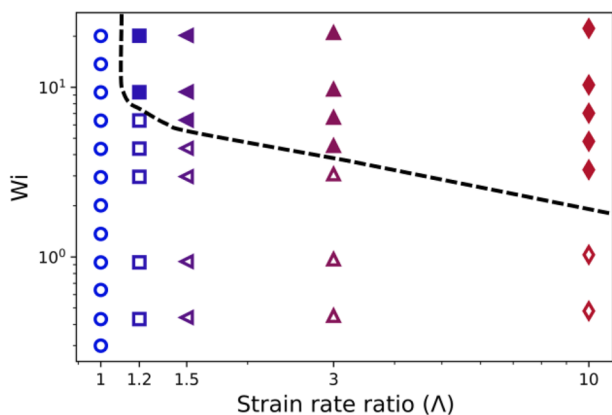


**FIG. 14.** Presence of the nematic phase in biaxial flows of varying  $\Lambda$  and  $Wi$ . Filled symbols represent the presence of a nematic phase, and empty symbols represent an absence of a nematic phase. The black dotted line is shown as a guide to the eye.

as the strain rate ratio increases, suggesting that such nematic domains are stabilized by more anisotropic, or non-equibiaxial, flow conditions. This idea is supported by looking at extremes of anisotropy in flow. Equibiaxial flow, which is the most isotropic, fails to show nematic phase formation even at the highest  $Wi$  studied. On the other hand, uniaxial flow shows nematic phase formation at  $Wi = 2.31$ ,<sup>22</sup> which is lower than for all biaxial flows studied here. Thus, flows with a higher strain rate ratio not only give a higher average Kuhn segment order but also are more efficient in the formation of nematic order domains within the melt.

#### IV. CONCLUSION

We performed NEMD simulations to study FEN under biaxial flows. Varying the strain rate ratio ( $\Lambda$ ), we observed a variety of orientations in the melt. These orientations range from low orientation in equibiaxial flows to high orientation in anisotropic biaxially flows, asymptotically approaching uniaxial flow for large values of

the strain rate ratio. Thus, biaxial extensional flows (BEFs) provide a good candidate to test FEN models. It is found that a model based on the Kuhn segment conformation tensor best explains FEN for all flow conditions. The stress-optical rule fails for BEF, and consequently, the model based on the extra stress tensor does not fit the data. Segmental orientation at the Kuhn segment scale can be obtained by melt birefringence studies, allowing for experimental validation of this model.

An NEMD study allows us to study the post-critical nuclei in detail and observe orientation and shape. We show that flow greatly influences the direction of crystal stems. Equibiaxial flows introduce randomness in orientation within the plane of extension, whereas asymmetric flows tend to orient all nuclei in one direction. We also observe that nuclei are largely spherical even for strong and anisotropic flows. Thus, nuclei do not show evidence of change in shape up to the sizes studied here. Hence, any change in morphology observed in experiments must occur at larger length scales than the ones studied here.

We are also able to show nematic phase formation in melt for biaxial flows that are asymmetric enough. Equibiaxial flows behave differently and fail to show the formation of a nematic phase. This nematic phase is also shown to nucleate preferentially. Thus, we can say that FEN occurs through the formation of more ordered parts in the melt phase. Our observations agree with other FEN and FIC studies conducted in the literature. From these observations, one can say that biaxial flows (especially equibiaxial) behave differently from uniaxial or shear flows previously studied. They orient melt and crystal stems differently and may not form a nematic phase. Thus, these flows must be treated appropriately in FEN experiments, simulations, and models.

#### SUPPLEMENTARY MATERIALS

Additional information and images are provided as the supplementary material in a separate file.

#### ACKNOWLEDGMENTS

The authors gratefully acknowledge support from Dow through the University Partnership Initiative. The authors also acknowledge

the Lamot du Pont Chair in Chemical Engineering to G.C.R. for funding of this work.

## AUTHOR DECLARATIONS

### Conflict of Interest

The authors have no conflicts to disclose.

## Author Contributions

**Chinmay S. Gangal:** Formal analysis (lead); Investigation (lead); Software (lead). **Gregory C. Rutledge:** Conceptualization (lead); Supervision (lead).

## DATA AVAILABILITY

The data that support the findings of this study are available from the corresponding author upon reasonable request.

## REFERENCES

- S. S. Sheiko and S. N. Magonov, *Polymer Science: A Comprehensive Reference, 10 Volume Set* (Elsevier, 2012), pp. 559–605.
- H. Janeschitz-Kriegl, *Crystallization Modalities in Polymer Melt Processing* (2010).
- K. L. Kearns, J. Scherzer, M. Chyasnachyus, D. Monaenkova, J. Moore, R. L. Sammler, T. Fielitz, D. A. Nicholson, M. Andreev, and G. C. Rutledge, “Measuring flow-induced crystallization kinetics of polyethylene after processing,” *Macromolecules* **54**, 2101 (2021).
- P. C. Roozmond, M. van Drongelen, and G. W. N. Peters, “Modeling flow-induced crystallization,” in *Polymer Crystallization II. Advances in Polymer Science*, Vol. 277, edited by F. Auriemma, G. Alfonso, and C. de Rosa (Springer, Cham, 2016).
- R. S. Graham and P. D. Olmsted, “Coarse-grained simulations of flow-induced nucleation in semicrystalline polymers,” *Phys. Rev. Lett.* **103**(11), 115702 (2009).
- H. Janeschitz-Kriegl, “Some remarks on flow induced crystallization in polymer melts,” *J. Rheol.* **57**(4), 1057–1064 (2013).
- E. Ratajski and H. Janeschitz-Kriegl, “Flow-induced crystallization in polymer melts: On the correlation between nucleation and specific work,” *Polym. Bull.* **68**(6), 1723–1730 (2012).
- A. Mahendrasingam, C. Martin, W. Fuller, D. J. Blundell, R. J. Oldman, and J. L. Harvie *et al.*, “Effect of draw ratio and temperature on the strain-induced crystallization of poly (ethylene terephthalate) at fast draw rates,” *Polymer* **40**, 5553–5565 (1999).
- I. Coccorullo, R. Pantani, and G. Titomanlio, “Spherulitic nucleation and growth rates in an iPP under continuous shear flow,” *Macromolecules* **41**(23), 9214–9223 (2008).
- L. Fernandez-Ballester, T. Gough, F. Meneau, W. Bras, F. Ania, F. J. Balta-Calleja, and J. A. Kornfield, “Simultaneous birefringence, small- and wide-angle X-ray scattering to detect precursors and characterize morphology development during flow-induced crystallization of polymers,” *J. Synchrotron Radiat.* **15**(2), 185–190 (2008).
- Y. Zhao, K. Hayasaka, G. Matsuba, and H. Ito, “In situ observations of flow-induced precursors during shear flow,” *Macromolecules* **46**(1), 172–178 (2013).
- J. Kornfield, S. Kimata, T. Sakurai, Y. Nozue, T. Kasahara, N. Yamaguchi, T. Karino, and M. Shibayama, “Molecular aspects of flow-induced crystallization of polymers,” *Prog. Theor. Phys. Suppl.* **175**, 10–16 (2008).
- S. L. Wingstrand, M. Van Drongelen, K. Mortensen, R. S. Graham, Q. Huang, and O. Hassager, “Influence of extensional stress overshoot on crystallization of LDPE,” *Macromolecules* **50**(3), 1134–1140 (2017).
- R. S. Graham, “Understanding flow-induced crystallization in polymers: A perspective on the role of molecular simulations,” *J. Rheol.* **63**(1), 203–214 (2019).
- A. Jabbarzadeh and R. I. Tanner, “Crystallization of alkanes under quiescent and shearing conditions,” *J. Non-Newtonian Fluid Mech.* **160**(1), 11–21 (2009).
- P. C. Roozmond, R. J. A. Steenbakkens, and G. W. M. Peters, “A model for flow-enhanced nucleation based on fibrillar dormant precursors,” *Macromol. Theory Simul.* **20**(2), 93–109 (2011).
- M. Anwar, J. T. Berryman, and T. Schilling, “Crystal nucleation mechanism in melts of short polymer chains under quiescent conditions and under shear flow,” *J. Chem. Phys.* **141**, 124910 (12) (2014).
- W. Zhang and R. G. Larson, “Direct all-atom molecular dynamics simulations of the effects of short chain branching on polyethylene oligomer crystal nucleation,” *Macromolecules* **51**(13), 4762–4769 (2018).
- C. Baig and B. J. Edwards, “Atomistic simulation of crystallization of a polyethylene melt in steady uniaxial extension,” *J. Non-Newtonian Fluid Mech.* **165**(17–18), 992–1004 (2010).
- A. Koyama, T. Yamamoto, K. Fukao, and Y. Miyamoto, “Molecular dynamics simulation of polymer crystallization from an oriented amorphous state,” *Phys. Rev. E* **65**(5), 050801 (2002).
- D. A. Nicholson and G. C. Rutledge, “An assessment of models for flow-enhanced nucleation in an *n*-alkane melt by molecular simulation,” *J. Rheol.* **63**(3), 465–475 (2019).
- D. A. Nicholson and G. C. Rutledge, “Flow-induced inhomogeneity and enhanced nucleation in a long alkane melt,” *Polymer* **200**, 122605 (2020).
- M. Cakmak, M. Hassan, E. Unsal, and C. Martins, “A fast real time measurement system to track in and out of plane optical retardation/birefringence, true stress, and true strain during biaxial stretching of polymer films,” *Rev. Sci. Instrum.* **83**(12), 123901 (2012).
- M. K. Hassan and M. Cakmak, “Strain-induced crystallization during relaxation following biaxial stretching of PET films: A real-time mechano-optical study,” *Macromolecules* **48**, 4657 (2015).
- X. Chen, L. Meng, W. Zhang, K. Ye, C. Xie, D. Wang, W. Chen, M. Nan, S. Wang, and L. Li, “Frustrating strain-induced crystallization of natural rubber with biaxial stretch,” *ACS Appl. Mater. Interfaces* **11**, 47535 (2019).
- Q. Zhang, R. Zhang, L. Meng, Y. Lin, X. Chen, X. Li, W. Zhang, and L. Li, “Biaxial stretch-induced crystallization of poly(ethylene terephthalate) above glass transition temperature: The necessary of chain mobility,” *Polymer* **101**, 15–23 (2016).
- C. Nie, F. Peng, T. Xu, Y. Ding, J. Sheng, W. Chen, and L. Li, “Biaxial stretch-induced crystallization of polymers: A molecular dynamics simulation study,” *Macromolecules* **54**, 9794 (2021).
- A. K. Doufas and A. J. Mchugh, “Simulation of film blowing including flow-induced crystallization,” *J. Rheol.* **45**(5), 1085 (2001).
- M. Bullwinkel, G. A. Campbell, D. H. Rasmussen, J. Krexa, and C. J. Brancewitz, “Crystallization studies of LLDPE during tubular blown film processing,” *Int. Polym. Process.* **16**(1), 39–47 (2001).
- M. van Drongelen, D. Cavallo, L. Balzano, G. Portale, I. Vittorias, W. Bras, G. C. Alfonso, and G. W. M. Peters, “Structure development of low-density polyethylenes during film blowing: A real-time wide-angle X-ray diffraction study,” *Macromol. Mater. Eng.* **299**(12), 1494–1512 (2014).
- W. Paul, D. Y. Yoon, and G. D. Smith, “An optimized united atom model for simulations of polymethylene melts,” *J. Chem. Phys.* **103**(4), 1702–1709 (1995).
- N. Waheed, M. S. Lavine, and G. C. Rutledge, “Molecular simulation of crystal growth in *n*-eicosane,” *J. Chem. Phys.* **116**(5), 2301–2309 (2002).
- N. Waheed, M. J. Ko, and G. C. Rutledge, “Molecular simulation of crystal growth in long alkanes,” *Polymer* **46**(20), 8689–8702 (2005).
- P. Yi and G. C. Rutledge, “Molecular origins of homogeneous crystal nucleation,” *Annu. Rev. Chem. Biomol. Eng.* **3**, 157–182 (2012).
- P. Yi and G. C. Rutledge, “Molecular simulation of bundle-like crystal nucleation from *n*-eicosane melts,” *J. Chem. Phys.* **135**(2), 024903 (2011).
- P. Yi, C. R. Locker, and G. C. Rutledge, “Molecular dynamics simulation of homogeneous crystal nucleation in polyethylene,” *Macromolecules* **46**(11), 4723–4733 (2013).
- R. Ranganathan, V. Kumar, A. L. Brayton, M. Kröger, and G. C. Rutledge, “Atomistic modeling of plastic deformation in semicrystalline polyethylene: Role

- of interphase topology, entanglements, and chain dynamics," *Macromolecules* **53**(12), 4605–4617 (2020).
- <sup>38</sup>A. P. Thompson, H. M. Aktulga, R. Berger, D. S. Bolintineanu, W. M. Brown, P. S. Crozier, P. J. in 't Veld, A. Kohlmeyer, S. G. Moore, T. D. Nguyen, R. Shan, M. J. Stevens, J. Tranchida, C. Trott, and S. J. Plimpton, "LAMMPS - A flexible simulation tool for particle-based materials modeling at the atomic, meso, and continuum scales," *Comput. Phys. Commun.* **271**, 108171 (2022).
- <sup>39</sup>D. A. Nicholson and G. C. Rutledge, "Molecular simulation of flow-enhanced nucleation in *n*-eicosane melts under steady shear and uniaxial extension," *J. Chem. Phys.* **145**(24), 244903 (2016).
- <sup>40</sup>M. Dobson, "Periodic boundary conditions for long-time nonequilibrium molecular dynamics simulations of incompressible flows," *J. Chem. Phys.* **141**(18), 184103 (2014).
- <sup>41</sup>T. A. Hunt, "Periodic boundary conditions for the simulation of uniaxial extensional flow of arbitrary duration," *Mol. Simul.* **42**(5), 347–352 (2016).
- <sup>42</sup>M. Tuckerman, B. J. Berne, and G. J. Martyna, "Reversible multiple time scale molecular dynamics," *J. Chem. Phys.* **97**(3), 1990–2001 (1992).
- <sup>43</sup>G. Ungar, J. Stejny, A. Keller, I. Bidd, and M. C. Whiting, "The crystallization of ultralong normal paraffins: The onset of chain folding," *Science* **229**(4711), 386–389 (1985).
- <sup>44</sup>P. Yi and G. C. Rutledge, "Molecular simulation of crystal nucleation in *n*-octane melts," *Phys. J. Chem.* **131**, 134902 (2009).
- <sup>45</sup>A. Bourque, C. R. Locker, and G. C. Rutledge, "Molecular dynamics simulation of surface nucleation during growth of an alkane crystal," *Macromolecules* **49**(9), 3619–3629 (2016).
- <sup>46</sup>M. Rubinstein and R. H. Colby, *Polymer Physics* (Oxford University Press, 2003).
- <sup>47</sup>L. J. Fetters, D. J. Lohse, and R. H. Colby, in *Physical Properties of Polymers Handbook*, 2nd ed., edited by J. E. Mark (Springer US, 2007), pp. 447–454.
- <sup>48</sup>M. Nafar Sefiddashti, B. J. Edwards, and B. Khomami, "Individual molecular dynamics of an entangled polyethylene melt undergoing steady shear flow: Steady-state and transient dynamics," *Polymers* **11**(3), 476 (2019).
- <sup>49</sup>V. A. Shneidman, "Communication: On nucleation statistics in small systems," *J. Chem. Phys.* **141**(5), 051101 (2014).
- <sup>50</sup>J. J. Gagnepain and C. Roques-Carmes, "Fractal approach to two-dimensional and three-dimensional surface roughness," *Wear* **109**, 119–126 (1986).
- <sup>51</sup>X. Tang, J. Yang, F. Tian, T. Xu, C. Xie, W. Chen, and L. Li, "Flow-induced density fluctuation assisted nucleation in polyethylene," *J. Chem. Phys.* **149**(22), 224901 (2018).